An in vitro model for the development of mature bone containing an osteocyte network

Iordachescu, Alexandra; Amin, Harsh; Rankin, Sara; Williams, Richard; Yapp, Clarence ; Bannerman, Alistair; Pacureanu, Alexandra; Addison, Owen; Hulley, Philippa; Grover, Liam

Link to publication on Research at Birmingham portal

An In Vitro Model for the Development of Mature Bone Containing an Osteocyte Network

Alexandra Iordachescu,* Harsh D. Amin, Sara M. Rankin, Richard L. Williams, Clarence Yapp, Alistair Bannerman, Alexandra Pacureanu, Owen Addison, Philippa A. Hulley, and Liam M. Grover

Bone is a dynamic tissue that remodels continuously in response to local mechanical and chemical stimuli. This process can also result in maladaptive ectopic bone in response to injury, yet pathological differences at the molecular and structural levels are poorly understood. A number of in vivo models exist but can often be too complex to allow isolation of factors which may stimulate disease progression. A self-structuring model of bone formation is presented using a fibrin gel cast between two calcium phosphate ceramic anchors. Femoral periosteal cells, seeded into these structures, deposit an ordered matrix that closely resembles mature bone in terms of chemistry (collagen:mineral ratio) and structure, which is adapted over a period of one year in culture. Raman spectroscopy and X-ray diffraction confirm that the mineral is hydroxyapatite associated with collagen. Second-harmonic imaging demonstrates that collagen is organized similarly to mature mouse femora. Remarkably, cells differentiated to the osteocyte phase are linked by canaliculi (as demonstrated with nano-computed tomography) and remained viable over the full year of culture. It is demonstrated that novel drugs can prevent ossification in constructs. This model can be employed to study bone formation in an effort to encourage or prevent ossification in a range of pathologies.

1. Introduction

Osseous tissue forms in various physiological circumstances, ranging from normal bone development and callus-mediated fracture repair, to pathological heterotopic bone formation in extra-skeletal tissues, as seen following muscle trauma, traumatic brain and spinal cord injury, surgical procedures of the hip and knee; and in genetic conditions such as *fibrodysplasia ossificans progressiva* (FOP).[1–9] These contexts, normal or otherwise, share fundamental characteristics at many levels, including molecular (overexpression of bone morphogenic proteins, BMPs), cellular (a set of progenitor cells that commits to an osteoblastic lineage) and biomechanical (translation of the mechanical forces into structured and organized bone).[3,10–15] However, there are still significant gaps in our understanding of these events and in particular few models allow long-term

A. Iordachescu, Dr. R. L. Williams, Dr. A. Bannerman, Prof. L. M. Grover
School of Chemical Engineering
University of Birmingham
Edgbaston, Birmingham B15 2TT, UK
E-mail: A.Iordachescu@bham.ac.uk

A. Iordachescu, Dr. C. Yapp, Dr. P. A. Hulley
Botnar Research Centre (NDORMS)
University of Oxford
Old Road, Headington, Oxford OX3 7LD, UK

Dr. H. D. Amin, Dr. S. M. Rankin
Inflammation, Development and Repair
National Heart & Lung Institute
Faculty of Medicine
Imperial College London
London SW7 2AZ, UK

Dr. H. D. Amin, Dr. S. M. Rankin
Centre for Blast Injury Studies
Department of Bioengineering
Imperial College London
London SW7 2AZ, UK

Dr. C. Yapp
Department of Cell Biology
Harvard Medical School
240 Longwood Ave, Boston, MA 02115, USA

Dr. A. Pacureanu
European Synchrotron Radiation Facility
Beamline Groups Unit
71 avenue des Martyrs, 38000 Grenoble, France

Prof. O. Addison
School of Dentistry
University of Birmingham
5 Mill Pool Way, Edgbaston, Birmingham B5 7EG, UK

**ADVANCED
SCIENCE NEWS**
www.advancedsciencenews.com

**ADVANCED
BIOSYSTEMS**
www.adv-biosys.com

physicochemical characterization of mature mineral production and the effect of this changing environment on incorporated cells. There are also several modalities to recreate pathological ossifications in animal models, including the overexpression or inhibition of molecular osteoinductive factors, trauma induction, and heterotopic implantation.[16–18] However, some of these models are not fully representative of the pathological states, requiring the use of a large number of animals; or are too complex to allow the isolation of individual contributing factors in early phase bone formation, which makes it objectively difficult to answer some essential questions on biological ossification.[16]

Developing novel ways to produce ossified tissue is essential for several scientific reasons. From a biological perspective, new models will help to develop a deeper understanding of the fundamental processes underlying both early bone development and the pathological ossification events following trauma or injury.[4,5] New approaches to develop bone-like materials are also required for the augmentation of bone defects and ultimately the replacement and surgical transplantation of tissue grafts.[1,19–21] In this context, the present work focused on developing a new, biological model of bone tissue formation, which would allow long term, whole construct testing of potential therapeutic drugs or of anabolic factors in a less complex environment. The aim was to develop a system that could in future be easily manipulated biochemically and biomechanically to simulate the ossification microenvironment encountered in both normal and pathological environments and that could ultimately be applied to investigate both biological and physical research questions. To develop this system, we used osteoblastic cells extracted from the periosteum of rat femoral bones. Periosteum cells are the main determinants in the reparative phase of bone fracture healing, when they interact with the temporary fracture callus, which serves as a scaffold for the formation of new bone.[1,22–25] Furthermore, they have been associated with heterotopic ossification (HO) and have the ability to give rise to endochondral bone when implanted in muscle, and therefore may be central to this condition.[17,24,26] Following isolation, periosteum cells were seeded into fibrin hydrogels, which critically permit self-assembly and imaging of a de novo collagen matrix, and because as materials, fibrin scaffolds have structural and biochemical similarities to the microenvironment of the callus formed early in fracture healing.[27–29] Both cortical and trabecular bone show a similar matrix alignment at the microscale, which is essential for development and mechanical resistance. To mimic this important feature, the environment of the fracture callus was further emulated by introducing two calcium phosphate (CaP) anchors at the extremities of the culture dish. These anchors served to enhance retention of the forming matrix, which created tension forces centrally that encouraged alignment along the direction of force, as seen in bone.[30] Instead of providing the constructs with preformed hydroxyapatite (HA) anchors (similar to the main constituent of the inorganic component of bone), we have provided beta-tri-calcium phosphate (β-TCP)/brushite anchors as they were more soluble and hence could provide the tissues with a local source of calcium and phosphorus to aid in ossification. Over time, constructs self-structure from a homogenous polymer, in the form of fibrin, into aligned, heterogeneous structures. Samples were characterized over a period of 1 year in culture in terms of matrix organization, cell behavior, and mineralization using a combination of optical, spectroscopic, and chemical techniques.

We show here that antiosteogenic compounds can reverse the progression of ossification, indicating potential for interventional studies.

2. Results

2.1. Early Events

Early developmental events commence with remodeling of the callus-like matrix following cell attachment to the scaffolds. The presence of the two calcium phosphate anchors causes the matrix to contract around the two holding points (**Figure 1**a). Over time, this retention results in the formation of tension in the soft tissue between the two anchors, which causes alignment at the cellular and molecular level along the direction of the force (Figure 1b). The presence of the two anchors is essential for generating these structures as fibrin gels, which are seeded with cells but are not provided with anchors do not become organized by cells and contract randomly (Figures S3 and S4, Supporting Information).

The matrix starts to become mineralized from the bone-like anchor regions as early as 10 d, and these deposits grow over the subsequent days as mineral nodules form throughout the structure (Figure 1b). Mineralization nodules can be detected by whole-mount Alizarin Red staining as early as day 11, starting from the anchors (Figure 1b,c). The homogeneous matrix changes over the first three weeks in culture, with a visually distinct matrix advancing from the anchors toward the center until the structures appear radically different following extended periods of time (3 months) (Figure 1d).

As a negative control, we used a non-cell seeded fibrin-based structure (Figure 1a). Although some shrinkage and a level of dispersed calcification were noted in these structures, they did not exhibit the high levels of structural organization that were notable in our cell-seeded scaffold structures, suggesting that the embedded cells are critical to enabling the reorganization and subsequent mineralization of the bone-like structures.

2.2. Initiation and Development of Ossification

The evolution of mineral and matrix in constructs over time is presented in **Figure 2**, which contains microtomographic 3D reconstructions of early (12–15 d) and mature constructs (3 months–1 year) developed with periosteal cells. These high-resolution microtomographies, acquired at sequential time points, also revealed that mineralized matrix started forming in early stages at the calcium–phosphate extremities in the absence of further osteogenic supplementation (Figure 2a–c), and progressed with subsequent osteogenic supplementation throughout the entire length of the constructs, until the structures became fully ossified after approximately 3 months (Figure 2d,e). The initial fibrin structure became gradually replaced with greater-density matrix (Figure 2h–j), which after 3 months contained deposits of high density mineral independent of the main bone-like structure (Figure 2k,l). Thus, a combination of clinically relevant types of ossification were noticed in this system: the first type—starting from the bone-like ends—resembling fracture repair; as
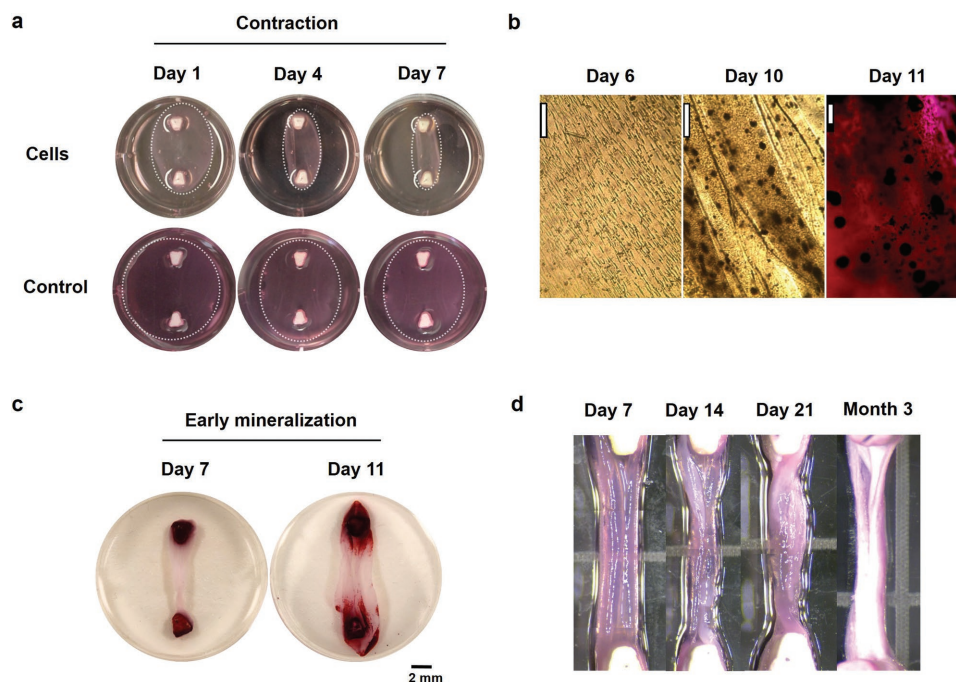
Figure 1. Early construct development. a) Fibrin scaffold is reorganized around the retention points over the first week in culture. Control constructs, developed without cells showed a small degree of contraction over 7 d, but remained as flat gels and did not assemble into 3D structures. b) Tensile forces between the two anchor points cause cell alignment before day 6 (left). Mineralization nodules are observed throughout the structure after 10 d (middle). c) Mineral deposits are not noticeable following 7 d but individual mineralization points can be observed 4 d later in the close proximity of the calcium phosphate source. Scale bars b = 50 μm (Day 6, 10), 200 μm (Day 11). d) Changes in the fibrin template are visually noticeable at 14 d, with a distinct matrix forming from the anchor regions toward the center, until the constructs appear to be fully covered with the new matrix at 3 months.
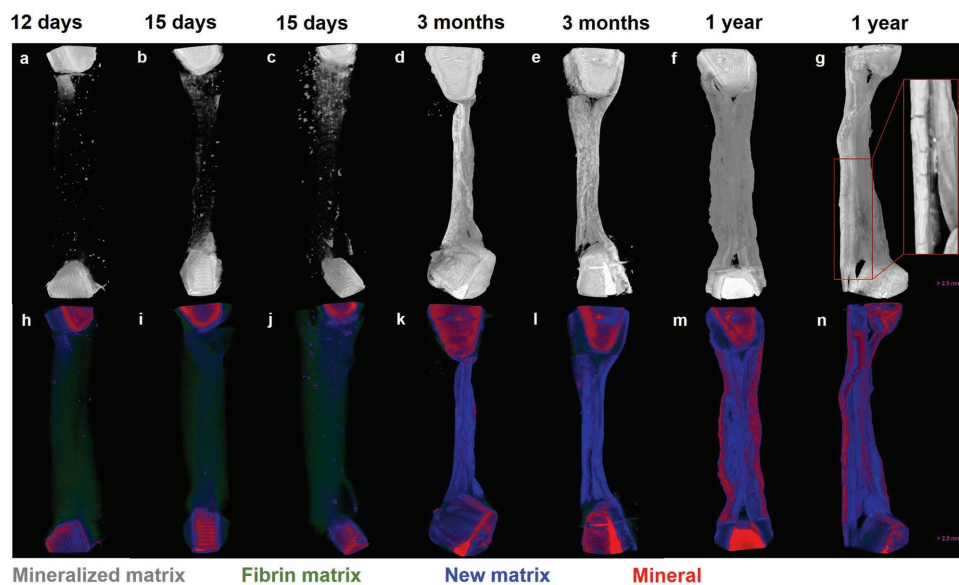
Figure 2. Development of mineralization and matrix over time. a–n) Reconstructed μCT images of early constructs (days 12–15, a–c/h–j) and mature constructs (3 months–1 year, d–g/k–n), illustrating the development of ossification over time. a–e) Mineralization starts at the anchors (a) and progresses over time throughout the entire length of the constructs (b,c) until the mineral covers the entire structure of constructs (d,e). Bottom panel presents color-coded versions of the constructs above, illustrating the development of the new matrix over time. The fibrin template (green), which predominates after j) 15 d, is progressively replaced over time with new matrix (blue) (h–j) until it becomes completely substituted after 3 months with the new, denser matrix, which also contains discrete deposits of high-density mineral (red) (k,l). Following a year in culture, the constructs contain considerable amounts of the high-density mineral (m,n). Cropped section illustrates the high-density material comprising the outer layer of constructs after a year in culture. Scale bars = 2.5 mm.

well as an isolated form, distant from the main bone-like structure, resembling mineral deposition in soft tissues as seen in ectopic ossification.[1,4,5] During the subsequent culture period up to one year, this new matrix becomes very dense and compact (Figure 2f,g/m,n), containing a high-proportion of mineral, particularly on the outside surface (Figure 2g).

2.3. New Matrix Characteristics

As indicated by tomographic analysis, constructs became mineralized through a process that was more complex than a simple calcification, i.e., the precipitation of calcium phosphate compounds on the fibrin matrix. Microtomographies indicated significant amounts of new, greater-density matrix colocalized with mineral deposits, which formed gradually throughout the culture period, indicating that a process of ossification was taking place. The nature and characteristics of these matrix components were analyzed through a combination of molecular, spectroscopic, and optical methods, which revealed an abundance of structural proteins associated with the extracellular matrix (ECM) of connective tissues. **Figure 3**a illustrates a comparison between the novel matrix observed in early stages (15 d) using μCT, and a high-resolution compositional Raman map developed based on the signal corresponding to one of the organic components identified in abundance, CH_2 (1447 cm^{-1}), indicative of collagen. The latter analysis revealed that a higher amount of this compound was distributed in a similar pattern observed with CT, at this equivalent time point. In bone, collagen is produced by osteoblastic cells during the assembly of the ECM and accounts for ≈90% of the organic component.[31] As such, its simultaneous deposition with the early mineral can be used as an indication of early ossification. Spectral analysis

of constructs which had just completed undergoing the contraction phase (7 d), revealed that the CH_2 band was accompanied by other bands such as amides I and III (1646 and 1316 cm^{-1}, respectively), proline and hydroxyproline (861 and 872 cm^{-1}, respectively), major components of collagen, and later, at day 12, by phosphate compounds in the central and interface regions, indicative of mineral formation and co-localized with the organic components (Figure 3b).[32] All the mineral detected using Raman spectroscopy at these early time points was different from the anchor material (Figure S5, Supporting Information), the majority being octacalcium phosphate (OCP, 954 cm^{-1}). OCP is thought to be an intermediate in hydroxyapatite formation in bones, enamel, and dentin and its presence as an intermediate phase in the formation of bone and dentin mineral has been a subject of great debate over the past decades. It has more recently been confirmed and described as taking place during in vivo mineralized tissue formation and in pathological dental and renal calcifications.[33–36] It has also been identified using similar Raman spectroscopy analysis in cultured calvarial bone tissue explants.[37] The presence of a novel phosphate phase in our system suggests a cell-mediated mineralization, but also indicates an advantage of our system in terms of the ability to simulate the temporal evolution of bone mineral.

At the end of an initial month in culture, a regime of full osteogenic supplementation was commenced, containing additional ascorbate, β-glycerophosphate, and dexamethasone. The purpose of this additional supplementation was to encourage ossification to progress more rapidly towards the center, at a point when the matrix was robust enough to maintain integrity during the rapid dissolution of the remaining fibrin caused by the new matrix replacement. Raman spectroscopic analysis performed following 2 months of supplementation revealed the presence of the complete set of peaks that have been reported
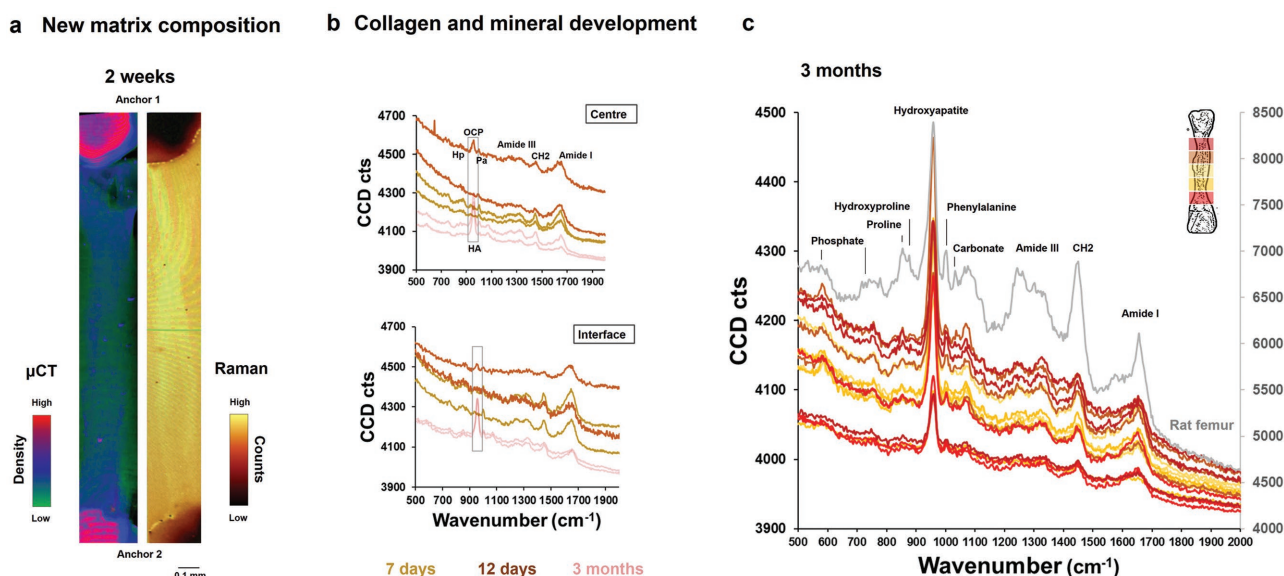
Figure 3. Chemical characteristics of the newly forming matrix. a) Comparison of a micro-CT reconstruction and a high-resolution Raman map, developed based on the CH_2 peak (1447 cm^{-1}) showing a similar distribution of the denser, newly forming matrix in constructs which are 2 weeks old. b) As early as day 7 (yellow), peaks corresponding to collagen can be detected, including amide I, III, CH_2, but also hydroxyproline (Hp) and phenylalanine (Pa). 5 d later (day 12, brown), small phosphate peaks corresponding to OCP start to emerge in the central and interface regions. Spectra from mature (3 month constructs, pink) are provided for comparison. c) Spectra from spatially distinct regions from a mature construct (3 months) showing in all cases a strong hydroxyapatite content colocalized with all the components associated with collagen. Spectra contain all peaks detectable in bone using this technique.

to be present in mature bone, and in all regions investigated, including the center (Figure 3c).[32,38] Interestingly, the mineral detected at this time point was the complex bone hydroxyapatite (957–962 cm^{-1}), suggesting a maturation process from the intermediate phases, and was in all cases associated with collagen.

Figure 4. Development of the collagenous matrix in constructs. a,b) Images of 7 d constructs stained with Sirius Red for collagen. Left image illustrates high amounts of collagen in the marginal region adjacent to the brushite anchor; right image demonstrates collag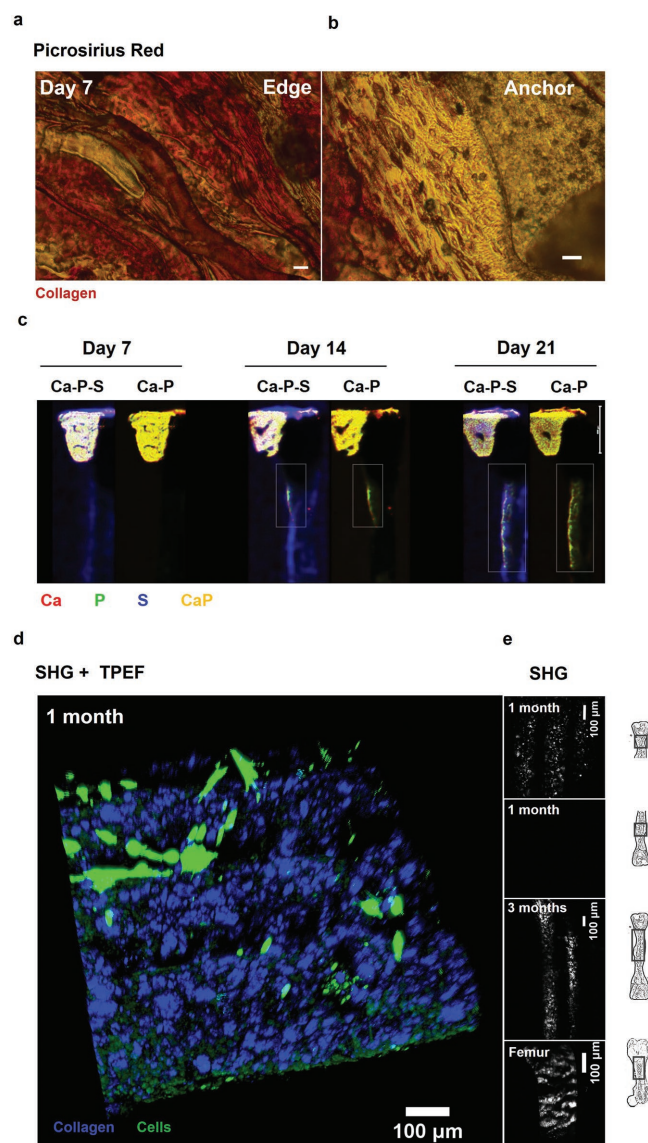en emerging from cell-like structures next to the anchor. Scale bars = 200 μm. c) Micro-XRF mapping of live constructs over 21 d, based on Ca and P, the inorganic components of bone and S, as an indicator of the organic matrix. Maps show the progression and co-localization of Ca and P from the anchor towards the center during this period of development up to one month. Scale bar = 4mm. d) An example of a 3D reconstruction of cells (TPEF) and collagen (SHG), simultaneously visualized in 1 month constructs. Collagen is present in "pocket"-like deposits. Scale bars = 100 μm. e) SHG visualization of collagen in distinct regions at different time points. Collagen is abundant around the anchor areas, but not detected in the central region at 1 month. Over the subsequent 2 months, the collagenous matrix extends into the tissue at the mm level, displaying a level of organization similar to murine femora (bottom image).

In terms of localization and organization of collagen in constructs, as early as day 7, collagen was detected using whole-mount picrosirius red staining, abundantly around the edges in the vicinity of the two anchors (**Figure** 4a) and adjacent to the anchors, where it appeared to emerge from cell-like structures (Figure 4b). As mineral deposits composed of calcium phosphate advance toward the center during the first month of culture (Figure 4c), the organic matrix progresses as well. Multiphoton microscopy was similarly employed to image collagen in 3D in live constructs by making use of the nonlinear optical effect known as second-harmonic generation generated exclusively by collagen when exposed to a laser of an infrared/near-infrared wavelength (Figure 4d; Figure S6, Supporting Information). Where structural information was necessary, such as the spatial dynamics between osteoblasts and their secreted matrix protein, second harmonic imaging was used in combination with an additional high-resolution optical technique, two-photon excited fluorescence (TPEF), which allowed the simultaneous visualization of collagen and viable cells, stained with a cell-permeant fluorescent dye (Calcein acetoxymethyl (AM)), at a cellular resolution but over the tissue length scale.[39] 3D analysis of constructs that were cultured for approximately one month showed significant deposits of collagen arranged in pocket-like structures in the interface regions, surrounded by cells (Figure 4d illustrates an example). Further analysis using second harmonics (Figure 4e) revealed that the central region of constructs did not contain detectable deposits of collagen at this time point, indicating that the ossification had not progressed as far up to that time point, but also that the collagen species secreted by cells centrally had not reached the sufficient maturity (i.e., the noncentrosymmetrical, triple-helical structure) required to reflect half the wavelength of the incoming laser and thus to be detected using this technique.[39,40]

Throughout the additional osteogenic regime, over the following months, ossification progressed at the mm scale until the two sides met centrally, showing the same pattern of organization of collagen pockets as observed in murine femoral bones (Figure 4e). Together, these results suggest a progressive deposition and maturation of mineralized collagen as seen in bone formation and fracture repair.[41]

2.4. Cellular Development in Constructs

During the culture period, the combination of biomechanical and chemical factors (i.e., presence of tensile forces, continuous source of calcium phosphates and osteogenic supplementation) ultimately had an influence on the specialization of the stem cells embedded in the constructs toward an osteoblastic lineage and subsequently recapitulated successive phases of ossification, including cell attachment to scaffold, clot remodeling, and matrix production.[42,43]

Optical analysis of the cellular morphological features during the months of culture revealed a pronounced restructuring of the cytoskeleton (Figure S7, Supporting Information), showing the formation of extensive projections characteristic of osteocytes and of long microcanals.

At the molecular level, cells present after a period of 5 months expressed the osteocytic marker sclerostin (SOST), a negative regulator of bone formation and an inhibitor of osteoblastic activity, on their outer membranes and in their
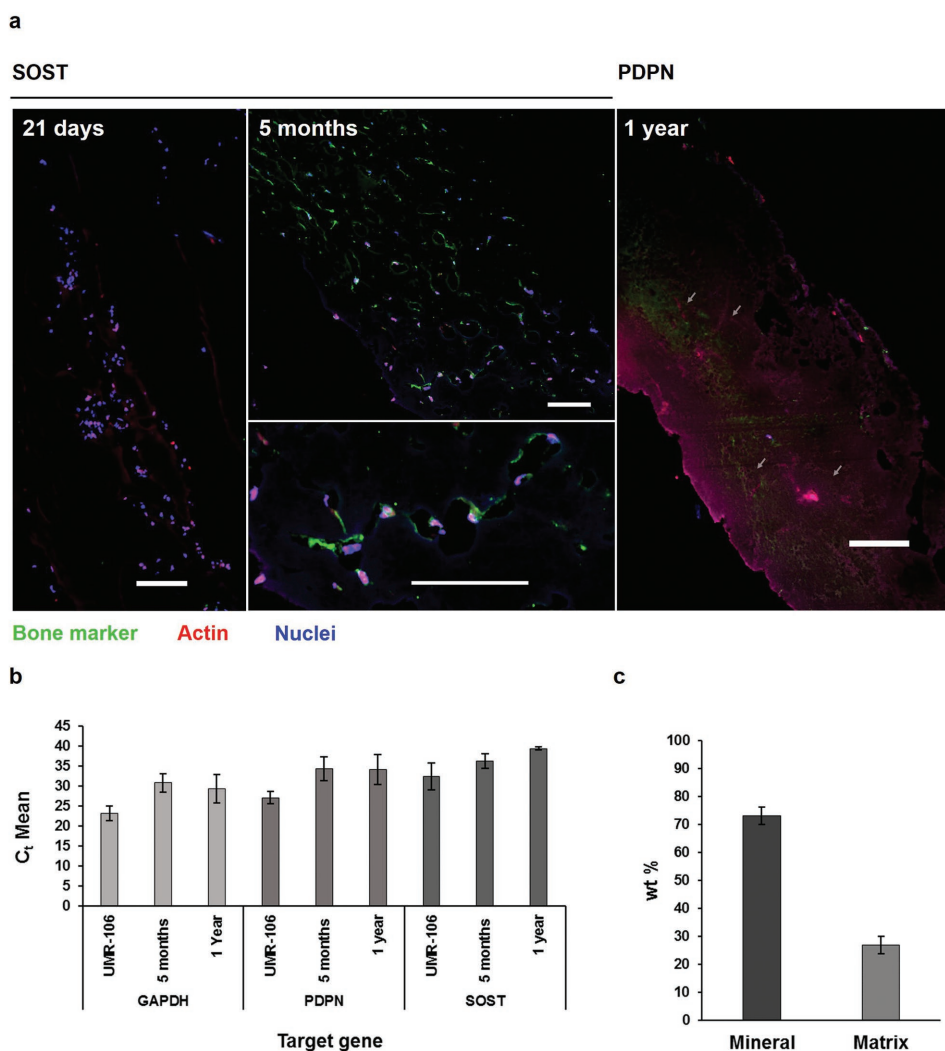
Figure 5. Detection and localization of bone markers in mature constructs. a) Immunohistochemistry of constructs, showing expression of osteocytic marker sclerostin on the surface of cells and in neighboring network-like structures at 5 months (middle). The matrix of 1-year-old constructs contains long networks, where podoplanin could be detected (right). Scale bars = 100 μm. b) mRNA for sclerostin and podoplanin was detected at these time points as well. Results are presented compared to a rat osteosarcoma cell line as positive control. UMR-106 produces sclerostin and podoplanin continuously. Please note cycle threshold (C_t) is inversely proportional to the amount of target nucleic acid in the sample. n_{pdpn} = 4 (umr, 5 m), 2 (1 year). n_{sost} = 4 (umr), 2 (5 m, 1 year). n_{gapdh} = 4 (umr, 5 m), 2 (1 year). c) The inorganic component of constructs following a year in culture equals approximately 70% of the total content, n = 3.

surroundings, which resembled cell networks (**Figure 5**a).[44–46] Further networks rich in sclerostin but also podoplanin (PDPN), a marker for the embedding osteoid osteocyte, and which is involved in reorganization of the cytoskeleton, could also be detected following the very extended culture time of 1 year (Figure 5a illustrates an example).[46,47] Sclerostin and podoplanin messenger RNA (mRNAs) were also detected at these late (5 months) and very late time points (1 year) (Figure 5b), suggesting an active role of the cells in building and remodeling the bony matrix.

Interestingly, the mineral to matrix ratio of these constructs at the latter time point reached a value similar to that of bone, with mineral occupying ≈70% of the total content (Figure 5c).[31] Moreover, the mineral was confirmed to be the mature bone hydroxyapatite using X-ray diffraction analysis (Figure S9, Supporting Information).[48] High-resolution optical

analysis of the cells in the most mature constructs (1 year) demonstrated further osteocytic morphological features. Cells at the surface of constructs, imaged using scanning electron microscopy (**Figure 6**a), appeared embedded in the heavily mineralized matrix. These cells contained a high number of large projections emerging from the cell bodies and reaching adjacent cells, as seen in bone.[49,50] Synchrotron radiation computed tomography (srCT), which enabled resolution down to the nanoscale, was used to visualize cells located below the surface, inside the constructs.[51,52] Figure 6b illustrates an example. The tomographic reconstruction further confirmed the presence of a complex canalicular network that linked the embedded cells, the first time that such elaborate structures have been attained using an in vitro culture. These channels were visualized using micro-X-ray fluorescence (μ-XRF) to provide a chemical map of the tissue structures (Figure 6c). Lacunae, which were shown
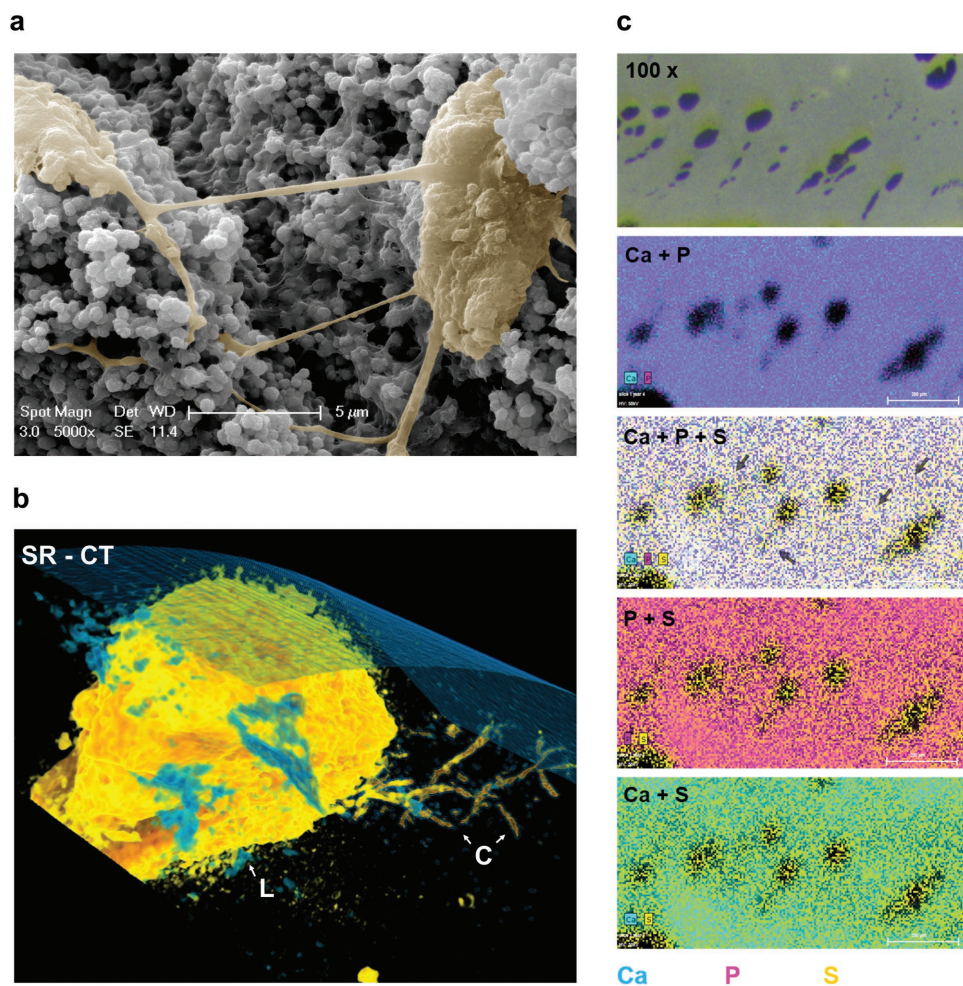
Figure 6. Development of bone cells in constructs. a) SEM images of cells in constructs after 12 months of culture, showing cells embedded in the significantly mineralized matrix. The main cellular structure in a has been false-colored to allow a better visualization. There are many podocytes embedded in the heavily mineralized matrix. Cells communicate through extensive projections. b) Synchrotron radiation computed tomography illustrating a typical osteocyte lacuna (L) with emerging canaliculi (C) that branch into the tissue. c) XRF maps based on S, Ca, P showing network-like structures throughout the matrix and connecting adjacent lacunar-like structures (arrows). Scale bars = 200 µm.

to house cells expressing osteocytic markers, were surrounded by a matrix rich in calcium and phosphate salts. The presence of a canalicular network was further supported by this analysis, which showed a sulfur-rich network (indicative of the presence of protein), which permeated through and between the lacunar structures (Figure 6c). Similar osteocytic structures, containing cellular DNA, were observed at earlier time points as well using histological analysis (Figure S8, Supporting Information).

Taken together, these results suggest that the microenvironment inside constructs, which developed into mature, mineralized collagen, reached a level of ossification similar to in vivo bone following long-term culture, which allowed the differentiation and survival of osteocytic cells over an extended, clinically useful period of time.

Osteocytes are extremely difficult to differentiate in vitro, as these mature cells form under complex conditions in their environment.[45] They are also very difficult to investigate in vivo due to their localization, embedded in lacuno-canalicular networks in hard bone, and their final stage differentiation into mitotically inactive cells.[45] Following isolation, culturing these

cells require complex supplementation regimes to prevent a quick de-differentiation into osteoblastic phenotypes. Although standard immortalized osteocyte cell lines (e.g., MLO-Y4) are available, they are not entirely representative due to reduced marker expression, particularly sclerostin.[53] As a consequence, to this date there are few models available for ex vivo or in vitro study of osteocytes and certainly none that allow for the long-term growth of these cells.

This work demonstrates that it is possible to fine-tune a primary osteoblastic cell population toward an osteocytic phenotype in a physiologically relevant system that develops into bone tissue at most levels, including cellularly (osteoblast and osteocyte development), compositionally and structurally (organized collagenous matrix production and mineralization). Although primary osteoblast to osteocyte cell transition has recently been reported in 3D by a few research groups, our model differs in the close recapitulation of complex in vivo conditions and in the self-structuring process as opposed to a preformed organic–inorganic matrix template (e.g., collagen scaffold with embedded HA particles).[45,54,55] As such, our constructs

survive over much greater periods of time (i.e., 12 months compared to a few weeks); as well as developing over a real tissue length scale. We have carried out a pilot study over 3 weeks in culture to test novel compounds that can inhibit the ossification process, obtaining promising results. In particular, treatment with compound CD1530, a nuclear retinoic acid receptor gamma agonist (RAR-γ) used in treating acquired and congenital heterotopic ossification, prevented the advancement of ossification toward the center by 99% compared to controls in a 21 d study (**Figure 7**).[56,57] Similarly, a second compound tested, LDN193189, which is a selective inhibitor of the BMP type I activin receptor-like kinase ALK2, ALK3, and which has been successfully used to reduce heterotopic ossification in transgenic murine models of FOP, when administered to constructs, was effective in reducing the mineralized matrix volume centrally by 70% compared to controls (Figure 7).[58]

The marked reduction in matrix volume following administration of these compounds was further confirmation that mineralization takes place through a cell-mediated route, as encountered during normal long bone formation, fracture repair, and heterotopic ossification.[57]
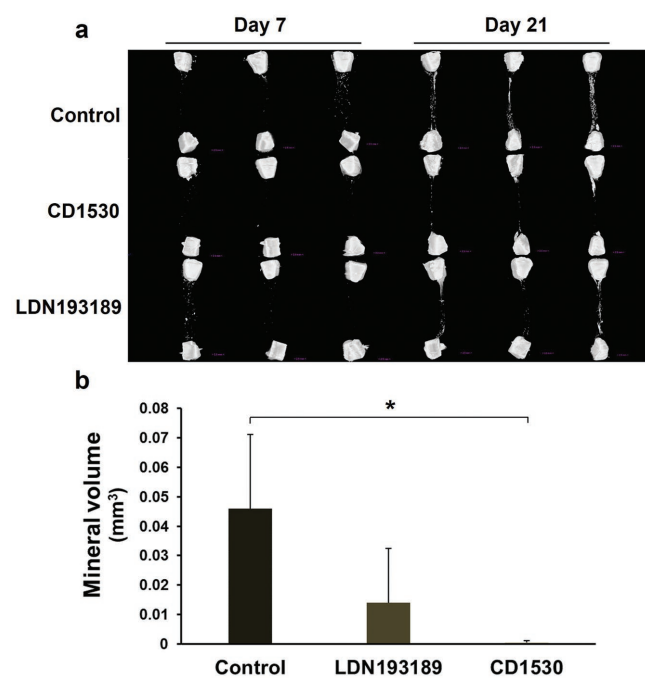

Figure 7. Ossification-inhibiting compounds decrease matrix and mineral formation in constructs. a) Administration of two inhibiting compounds in a pilot study lasting 21 d appeared to reduce the progression of ossification in treated constructs compared to controls. CD1530 (1×10^{-6} M) significantly reduced mineralized matrix formation following 21 d of culture compared to equivalent controls. LDN193189 (25×10^{-9} M) also appeared to be effective. b) Comparison of the mineral volume located in the central portion of constructs following 21 d of culture, quantified by morphometric CT analysis. Constructs treated with CD1530 showed an average of 99% less mineral in this region compared to controls, which was statistically significant, whereas the group treated with LDN193189 showed 70% less mineral, although not significant. Data are presented as means ± SD. *$p < 0.05$, $n = 3$.

3. Conclusion

Here, we demonstrated how simple homogeneous materials (fibrin) may be structured and modified by populations of cells to create complex tissues by making relatively simple geometrical and chemical modifications to the culture system. The composition of the tissues was probed using a suite of chemical analysis techniques that allowed us to identify the distribution and local organization of matrix components.

After even short periods of culture, the tissues were shown to be heterogeneous in composition and structure, with collagen and mineral distributed in spatially distinct regions (for a summary, see Figure S2 in the Supporting Information). Importantly, our Raman spectral data suggested that the mineral deposited within the tissue was associated with collagen as opposed to precipitated on the surface of the tissue. The mechanism of tissue formation was similar to a fracture callus and we demonstrated that the distribution of collagen and mineral within the tissue was similar to that found in mouse femora. We have further shown that the initial phosphate species convert to HA, as encountered in biological tissues. This transition can be recreated in our system via intermediate phases (such as OCP).

Our model displays promise for use in many research areas, ranging from tissue engineering and bone replacement materials, to heterotopic ossification research. It could also be a valuable tool for assessing material properties, such as the transition of harmful ions from medical devices into the surrounding tissues, in a realistic 3D environment. Moreover, it could serve as a screening platform for testing a wide range of drugs that suppress or enhance the ossification process. This means that our system could potentially reduce the number of animals required for skeletal research by providing an intermediate platform between in vitro and in vivo research.

Moreover, we briefly present here (Figure S10, Supporting Information) some examples showing the flexibility of this system in developing embedded cells of different human and animal skeletal origin (including primary chondrocyte and tendon cells). We also provide a brief example of our early work toward vascularizing the constructs (Figure S10c, Supporting Information), a step closer to mimicking the in vivo bone characteristics. Finally, we present an account of the wide range of cells which have already been tested in our system (Table S1, Supporting Information).

4. Experimental Section

Isolation of Primary Rat PO Cells: Femurs from left and right rat limbs were excised and surrounding muscular and connective tissue was removed. Femurs were stored in phosphate buffered saline (PBS) solution (pH 7.4; Gibco, Life Technologies, Thermo Fisher Scientific, UK) until use. Periosteal cells were extracted from the periosteum via enzymatic digestion using a cocktail containing 2.5 mg mL^{-1} collagenase I, 0.7 mg mL^{-1} collagenase II and 0.5 units per ml dispase I, in PBS (Gibco, Life Technologies, Thermo Fisher Scientific, UK). Bones were incubated with this solution at 37 °C for 1 h in a 5% CO_2 atmosphere. Following incubation, tubes containing bones and solution were shaken rigorously for 30 s to detach the remaining cells. Solutions were then pooled and filtered using 70 μm filters (Falcon, Becton Dickinson, UK). Cells were recovered using centrifugation

at 21 °C, 1400 rpm for 6 min. The supernatant was discarded and the resulting pellet was resuspended in 10 mL D20 growth medium (Dulbecco's modified Eagle medium (DMEM) containing 20% serum). Approximately 1 million PO cells from each bone were cultured for 10–12 d in D20 medium (Figure S1, Supporting Information).

Cell Lines: Cells originating from cell lines mouse calvarial osteoblasts (MC3T3-E1/2T3s) were obtained from the European Collection of Authenticated Cell Cultures and were cultured according to standard procedures in Minimal Essential Medium Eagle (MEM) Alpha Modification (10% fetal bovine serum, 1% P/S, 2.4% L-glutamine) (Sigma-Aldrich, Germany).

Tissue-Engineered Constructs: Constructs were developed by seeding fibrin hydrogels with osteoblastic cells, either periosteal cells from rat femurs, or from cell lines such as MC3T3-E1 or 2T3. The fibrin scaffolds were produced through the interaction of the normal plasma components thrombin and fibrinogen. Bovine-derived thrombin powder (Calbiochem, EDM Chemicals; 1KU) was reconstituted using 0.1% w v^{-1} bovine serum albumin (BSA) and 5 mL F12K Nutrient Mixture (1×) with Kaighn's modification (Gibco Life Technologies) to make a final concentration of 200 units per mL. Powdered bovine fibrinogen (Sigma Life Sciences) was reconstituted in F12K Nutrient Mixture (1×) with Kaighn's modification (Gibco Life Technologies) at a ratio of 20 mg mL^{-1}. Thrombin was added to a solution containing the cell culture medium (either DMEM or αMEM) at a ratio of 50 µL mL^{-1} solution. The antifibrinolytic agents aminohexanoic acid (200 × 10^{-3} M) and aprotinin (10 mg mL^{-1}) were added to the thrombin solution at a ratio of 2 µL mL^{-1} in order to reduce the degradation rate of the fibrin gel, in order for it to match the rate of new matrix formation so that the mechanical integrity of the tissue could be maintained over longer periods of time. Hydrogels were generated by mixing 500 µL thrombin solution with 200 µL fibrinogen. Thrombin cleaves small peptides from the fibrinogen chain, producing soluble fibrin monomers, which then cross-link into an insoluble, polymerized fibrin clot. Gels were allowed to polymerize for 30–40 min. Cells were seeded into the fibrin constructs immediately following gel polymerization; at a density of 100.000 per 2 mL of cell culture medium.

β-Tricalcium Phosphate Anchors: 2.5 g of β-TCP powder (<125 m particle size) was added per 1 mL of orthophosphoric acid (3.5 M) to generate a paste, composed of a mixture of brushite and β-TCP. The liquid mixture was poured into individual, preshaped wells of molds, placed on top of a shaking platform, to encourage uniform setting inside the shapes. 1.4 cm stainless steel insect pins (Austerlitz minutiens, Fine Science Tools, USA), with a diameter of 0.20 mm were inserted into the individual wells on the molds before the mixtures advanced into a solid state. The mixtures containing the pins were allowed to fully harden for 3–4 h and were sterilized overnight using UV light exposure, as well as with 70% EtOH for 30 min on the day of use. The final anchors had a trapezoidal shape and measured approximately 3 mm × 4 mm × 4 mm in height. The anchors were mounted on solidified silicone elastomer bases (1.5 mL of Sylgaard184, Dow Corning) placed at the bottom of individual wells on six-well culture dishes. Attachment was performed using the pins, using 2 anchors per well, which were applied at a distance of 1.5 cm from each other.

Osteogenic Supplementation of Periosteum Cell Constructs: Constructs developed with periosteum cells were supplemented following 1 month of culture with full osteogenic DMEM culture medium containing β-glycerophosphate (10 × 10^{-3} M), ascorbic acid (0.1 × 10^{-3} M), and dexamethasone (10 × 10^{-9} M) (Sigma Aldrich, Germany), to encourage new matrix deposition along the entire length of the constructs.

CD1530 and LDN193189 Supplementation: RAR-γ agonist CD1530 and ALK$_{2/3}$ inhibitor LDN193189 were administered in the culture medium of constructs at a concentration of 1 × 10^{-6} and 25 × 10^{-9} M, respectively. Starting with day 7 of culture, constructs received one dose every 2 d (6 doses total) of either CD1530 or LDN193189. Controls received an equivalent amount of dimethyl sulfoxide, which was used in drug dissolution.

Supplementation of Other Constructs: Following 7 d of development, the MC3T3-E1 constructs were supplemented with ascorbic acid

(250 × 10^{-6} M final concentration) and proline (50 × 10^{-6} M final concentration) every 2 d, to stimulate collagen deposition (Sigma Life Sciences, Germany).

Raman Spectroscopy: Confocal Raman spectroscopy was used to detect and spatially resolve specific chemical groups associated with mineralized collagen deposition through the constructs. Maps and spectra were acquired using a confocal Raman microscope (Alpha 300R, WITec, Ulm, Germany), equipped with an Acton SP2300 Imaging Monochromator/Spectrograph (Princeton Instruments, MA, USA), fitted with a 300 g mm^{-1} with 750 nm blazing grating, and a 785 nm 250 mW diode laser (XTRA II, Toptica photonics, Munich, Germany).

Spectra were acquired from various points on the constructs, including the anchor; the interface between the anchor and the soft tissue and the central portion, via a 20X (NA = 0.45) objective lens and using an integration time of 3 s and 20 accumulations. Data were accumulated and exported using the WITec Control software version 1.6 (WITec, Ulm, Germany).

Micro-Computed Tomography (µCT): X-ray microcomputed tomography allowed a nondestructive 3D visualization of constructs and offered detailed insight into the initiation and development of ossification.

A micro-computed tomography system (µCT) (SkyScan 1172, Bruker Instruments, Germany) was used to evaluate mineralization and matrix development in constructs over time. Constructs were removed from the culture medium and were placed vertically inside plastic tubes, on a rotating stage located at 260.650 mm distance from the X-ray source and 347.109 mm from the detector. High-resolution scans were performed at ambient pressure using the cone-beam imaging system, composed of a Hamamatsu X-ray source with a voltage of 80 kV and a tube current of 100 µA. The X-ray detector consisted of an 11 Mp X-ray camera of a 9.01 µm pixel size, generating images of 6.76 µm pixel size. 2D cross-section slices of the constructs were acquired at a rotation step of 0.2°, with two frames averaging per step and an exposure time of 1050 ms. Acquired images were 3D reconstructed using the Bruker micro-CT NRecon Software (v. 1.6.10.2). For removal of scanning artifacts, several reconstruction parameters were adjusted during reconstruction. The beam hardening parameter was set to a value of 30 to correct for the surface-to-depth density gradient caused by increased X-ray attenuation at the surface of the constructs. A ring artifact correction was set to a level of 9. The smoothing parameter was adjusted to a value of 4. These optimized, construct-specific settings were used for all time points investigated.

For constructs subjected to drug treatment, as these samples were less ossified and hence less dense, acquisition settings were adjusted to an X-ray voltage of 50 kV and a tube current of 100 µA; an image pixel size of 13 µm, with an exposure time of 510 ms, a rotation step of 0.4° and a frame averaging value of 2. Flat field correction was performed for image clarity and no ring artifact correction was applied.

Transfer functions were created in the CTVox software that allowed segmentation of the high density matrix components, as well as for creating color-coded versions of the components in the constructs. The same transfer function was used for all constructs in the same group of investigation.

Volumetric Analysis: Volumetric quantification of the mineral component was performed using morphometric analysis in the CTAn software (v. 1.13). 200 slices from equivalent regions in the central portions of control and drug treated constructs were isolated and a threshold of 220–255 was applied to segment the high density mineral component. 3D analysis of the segmented volume was performed and data was averaged to obtain the final volume in mm^3.

Synchrotron Radiation-Computed Tomography: srCT analysis was conducted on the nanoimaging beam line ID16 at the European Synchrotron Radiation Facility (ESRF) in Grenoble, France. Constructs were fixed with 4% formaldehyde and dried for 30 min at 50 °C. 5 mm samples of constructs were excised and placed on the rotating stage. Images were acquired at a resolution of 50 or 100 nm and a number of slices of 65–200 was acquired and used for 3D reconstruction.

Second Harmonic Imaging and Two-Photon Excitation Fluorescence: A multiphoton microscopy system was used to observe collagenous

matrix formation in constructs using the optical effect of second harmonic generation (SHG). To concomitantly visualize collagen and cells, constructs were stained with the fluorescent dye Calcein AM (Sigma-Aldrich, Germany) at a ratio of 2 µL mL^{-1} of Opti-MEM culture medium (Gibco, Thermo Fisher Scientific, USA) to assess viability and distribution of cells.

The microscopy system consisted of a Zeiss LSM710 NLO (Zeiss Gmbh, Germany) coupled to a Ti:Sapphire mode-locked Coherent Chameleon Vision II laser. Collagen and fluorescent cells were imaged using SHG and TPEF between 385–475 and 480–655 nm, respectively. Photons were collected through a 10× Plan Apo 0.45 N.A. and the two-photon laser was tuned at 860 nm. The presence of collagen was confirmed by spectral imaging and collecting the second harmonic signal at 430 nm via a 10× Plan Apo 0.45 N.A. or 40× Plan-Apo 0.95 N.A. objective. Where z-stacks were acquired, a slice interval of 6 µm was used. Images were visualized in ZEN 2009. Cell viability measurements were taken at different time points using Calcein AM, as described above and imaging was performed using either the Zeiss LSM710 NLO or a Leica DM2500/TCS SPE Confocal (Leica Microsystems, Wetzlar, Germany). Where z-stacks were acquired, a step size of 0.50 µm was used and excitation was performed using a 488 nm laser.

Elemental characterization Using Micro X-Ray fluorescence: A micro X-ray fluorescence system (M4 Tornado, Bruker Nano Gmbh, Berlin, Germany) was used to generate spatially resolved elemental maps of constructs and to investigate mineral and organic matrix distribution using the localization of Ca, P, and S in constructs.

The machine contains a rhodium µ-focus X-ray tube and a polycapillary lens, used to focus the X-rays to a spot size of 25 µm. Recordings were taken without sample processing, at room temperature and ambient pressure. The X-ray tube voltage used was 50 kV and tube current was 400 µA. µXRF spectra and maps from constructs of different ages were acquired using a 50 µm spot distance, 25 µm spot size, and 50 ms per pixel exposure time.

High-resolution elemental mapping of the lacunar structures and matrix of 1 year constructs was performed on flat, 4 µm thick slices (see Histoprocessing) using a spot size of 25 µm, distance of 5 µm, with 10 ms per pixel exposure time and 100 frame counts. Measurements were recorded under vacuum, at ≈800 mbar. Elemental maps were formed in real time by integrating the photon counts around the emission lines of: calcium (Kα_1 3.692 keV), phosphorus (Kα_1 2.010 keV), sulfur (Kα_1 2.309 keV), generating an image where pixel intensity was proportional to the number of X-ray counts/second per electronvolt (eV) from each measured point on the construct. Thus, pixel intensity increased with X-ray counts, with maximum pixel intensity normalized to the highest count rate per eV for each element of interest, across the entire construct.

Thermal Isolation of Mineral: Constructs were removed from culture and their calcium phosphate anchors were excised. Remaining tissues were dried at room temperature overnight and weighed using an Ohaus Pioneer Plus analytical balance (Ohaus, NJ, USA). Tissues were then introduced into a 900 °C hot oven for 13 h to remove organic matter (Carbolite CWF1300, Carbolite Gero, Hope Valley, United Kingdom). Following this period, the inorganic matter isolated was weighed and the percentage mineral content was calculated.

X-Ray Diffraction: X-ray diffraction was used to determine the crystalline composition of the samples. The crystals produced from the samples following 13 h of heating in a furnace were ground into fine powders with a marble mortar and pestle and carefully formed into a 10 mm wide thin circular layer on sticky tape. X-ray diffraction patterns of the mounted powders were then collected using with a Bruker D5000 X-ray diffractometer (Bruker ASX, Karlsruhe, Germany) using the Cu Kα_1 1.5406 Å line, with a 2θ range of 24.6° to 48°, a 0.02° step-size and a step time of 0.05 s per° leading to a total scan time of ≈1 h. Detected peaks were compared to JCPDS reference patterns to identify the crystalline phases in each sample. PDF 00-009-0432 and 00-012-0404 were used as reference patterns for hydroxyapatite and Whitlockite, respectively.

Scanning Electron Microscopy: 12 months-old constructs were fixed with 2.5% glutaraldehyde in phosphate buffered saline and dehydrated over several steps including immersion in ethanol of increasing concentrations and critical point drying using CO$_2$. Samples were coated with platinum and SEM images were acquired under vacuum using a Philips XL30 FEG ESEM at a resolution of 3 nm at 15 kV. Various cellular structures were colored using Adobe Photoshop CC 2015 (Adobe Systems Incorporated, CA, USA) to allow a better visualization.

Quantitative Polymerase Chain Reaction: 5 months ($n = 4$) and 12 months ($n = 2$) constructs were removed from culture media and the calcium phosphate anchors were cut out of the tissue and discarded. Tissues were snap frozen by submersion in liquid nitrogen for 1 min, then rapidly pulverized using a multisample biopulverizer (BioSpec Products Inc., OK, USA). mRNA extraction was performed using a Dynabeads mRNA DirectTM detection kit. The powdered tissue extract was lysed using vortex mixing and viscosity of the solution was reduced by DNA-shearing with a 21 gauge syringe needle. mRNA was isolated with oligo dT superparamagnetic beads (Dynabeads) using a Dynabeads MPC-S magnetic particle concentrator (Dynal AS Oslo, Norway) and cDNA synthesis was performed directly on the bead bound mRNA using a SuperScript Reverse Transcriptase kit (Invitrogen, Thermo Fisher Scientific, CA, USA). Quantitect primers (Qiagen, Manchester, UK) were used with Fast SYBR green master mix (Applied Biosciences, CA, USA) for rat podoplanin (QT00174706), sclerostin (QT00418558), glyceraldehyde 3-phosphate dehydrogenase (GAPDH) (QT00199633), and beta actin (QT00193473). Amplification of cDNA was performed using a ViiA 7 real-time PCR instrument (Applied Biosystems, CA, USA). As positive control, cells from an osteosarcoma cell line positive for SOST and PDPN, UMR-106, were used and mRNA was extracted and processed in an identical manner. Data were recorded and analyzed using the QuantStudio real-time PCR software, version 1.2 2015 (Applied Biosystems, CA, USA). In addition to no template controls, products were validated using melt point analysis to show a single high temperature melt point.

Histological Analysis of Whole Constructs: An Alizarin Red dye was used to chemically detect the presence of mineralization in constructs. Alizarin Red S powder (Sigma-Aldrich, Germany) was dissolved in distilled H$_2$O to a concentration of 40 × 10^{-3} M. The pH was adjusted to 4.2 with 10% (v v^{-1}) ammonium hydroxide (Fisher Scientific, USA). Constructs were fixed with 10% PFA for 30 min at room temperature. Following fixation, the constructs were rinsed in phosphate buffered saline solution (Sigma-Aldrich, Germany) to remove the excess PFA, and were inserted into 2 mL of Alizarin Red solution for 30 min at room temperature. Constructs were rinsed three times with PBS to remove unbound dye and were imaged using a CETI Inverso TC100 brightfield microscope (Medline Scientific, Oxon, United Kingdom) and a Zeiss Axio Lab A1 microscope (Carl Zeiss, Jena, Germany).

Sirius Red dye was used to detect collagen synthesis in constructs. Sirius Red dye (Direct Red 80, Sigma- Aldrich, Germany) was dissolved in saturated aqueous picric acid at a concentration of 1 mg mL^{-1}. Constructs were rinsed with PBS and fixed with 2 mL standard Bouin's fluid for 1 h at room temperature. The fixation fluid was aspirated and constructs were washed with dH$_2$O for 15 min. 2 mL of dye was added per construct and the recipients were placed on a plate shaker for 1 h (100 RPM). The excess liquid was removed and the unbound dye was removed by rinsing with 2 mL 0.01 N hydrochloric acid. Collagen deposits were visualized under the microscope.

Histoprocessing: For histology and immunohistochemistry, constructs were fixed in 10% neutral buffered formalin for 3 d, and were then embedded in paraffin wax blocks for sectioning. 4 µm thick paraffin tissue slices were produced using a Leica microtome (Leica Microsystems, Wetzlar, Germany).

Glass slides containing tissue sections were deparaffinized and rehydrated through subsequent washes with Neo-Clear (xylene substitute, Merck Millipore, Massachusetts, USA), twice for 5 min, 100% EtOH, 96% EtOH, and 70% EtOH twice for 30 s each time, followed

**ADVANCED
SCIENCE NEWS**

www.advancedsciencenews.com

**ADVANCED
BIOSYSTEMS**

www.adv-biosys.com

by a 1 min wash with dH$_2$O. Following the application of dyes, slides were prepared for long-term storage by washing with dH$_2$O followed by dehydration in ascending concentrations of EtOH, as follows: 70%, 96%, and 100% EtOH twice for 1 min, followed by a final wash with Neo-Clear, twice for 5 min. Slides were mounted using a water-free agent, Neo-Mount (Merck Millipore, Massachusetts, USA) for long-term storage. Tissue sections were imaged using a Leica DM500 microscope (Leica Microsystems, Wetzlar, Germany).

H&E Staining of Tissue Sections: A hematoxylin and eosin (H&E) stain was used in order to stain cell nuclei, cytoplasm, and the matrix of constructs. Hematoxylin staining solution was applied for 3 min and slides were washed under running tap water for 3 min. Eosin Y solution 0.5% was applied for 3 min. Samples were rinsed under running tap water for 30 s.

Immunohistological Analysis: Slides containing tissue sections were deparaffinized and rehydrated through subsequent washes with Neo-Clear (xylene substitute, Merck Millipore, Massachusetts, USA) and 100% EtOH twice for 3 min; followed by washes in 95% EtOH, 70% EtOH, and 50% EtOH for 3 min each time, followed by a wash with dH$_2$O. Antigen retrieval was performed using the water-bath immersion method, where the slides containing tissue sections were immersed in citrate buffer (10 × 10^{-3} M sodium citrate in dH$_2$O, pH 6, Abcam, Cambridge, United Kingdom) for 8 h. Slides were washed twice for 5 min in tris-buffered saline (TBS), which contained 0.025% Triton X-100 (Thermo Fisher Scientific, Massachusetts, USA). Tissue sections were blocked in medium containing 1% BSA and 10% normal serum in TBS from either donkey or goat, depending on the species of the secondary antibodies, for 2 h at room temperature. Primary rabbit antibodies against rat sclerostin (Abcam, Cambridge, United Kingdom), podoplanin (Abcam, Cambridge, United Kingdom) and collagen type I (Col I) (Thermo Fisher Scientific, Massachusetts, USA) were diluted to a concentration of 10 µg mL^{-1} in TBS with 1% BSA. Antibodies were applied to the slides and incubation was performed overnight at 4 °C. Samples were rinsed twice with TBS containing 0.025% Triton X-100, with gentle agitation. Secondary antibodies (donkey anti-rabbit or goat antirabbit) conjugated to Alexa Fluor 488 fluorophores, were diluted to 10 µg mL^{-1} (donkey) or 5 µg mL^{-1} (goat) in 1% BSA in TBS and were incubated with the slides for 1 h at room temperature. Following incubation, tissue sections were washed three times with TBS for 5 min. In order to check for nonspecific antibody binding, the steps listed above were performed on additional slides, without the addition of the primary antibodies Slides were washed with TBS containing 0.1% Triton X-100 for 5 min. Phalloidin (Thermo Fisher Scientific, Massachusetts, USA) conjugated to Alexa Flor 594 or 555 was used for cytoskeletal labeling. The phallotoxin was diluted to a concentration of 200 units per ml (6.6 × 10^{-6} M) and 3U were applied in TBS to each tissue-containing slide. Samples were washed with PBS twice. 4′,6-Diamidino-2-phenylindole was used for nuclear/DNA staining dissolved in mounting agent. Tissue sections were mounted with Pro-Long Diamond anti-fade permanent mountant (Thermo Fisher Scientific, Massachusetts, USA) for fluorescence preservation. Fluorescence images were acquired using an Olympus Fluoview FV1000 confocal laser scanning microscope (Olympus, Tokyo, Japan) equipped with a multi-line argon laser FV5-LAMAR/LAMAR-2 and a Helium–Neon Green Laser FV5-LAHEG-2/FV5-LAHEG. Images acquired from excitation at 405, 488, and 543 nm wavelengths were collected in individual channels and combined using the Fluoview FV10-ASW software, version 4.2 (Olympus, Tokyo, Japan).

Statistical Analysis: Measurements were acquired in triplicate and/or from a sample number of three constructs, unless otherwise indicated in the text. Raw data were not preprocessed (normalized/transformed) unless indicated otherwise. All data are presented as mean ± SD. Statistical analysis was performed using a one-tailed distribution t-test, with a heteroscedastic variance assumed. A *p* value lower than 0.05 was chosen for determining significance (MS Excel, Washington, USA). Percentage difference was calculated using the formula $X = (A - B)/A * 100$.

Supporting Information

Acknowledgements

Conflict of Interest

The authors declare no conflict of interest.

Keywords

[1] T. A. Einhorn, L. C. Gerstenfeld, *Nat. Rev. Rheumatol.* **2015**, *11*, 45.

[2] D. S. Edwards, J. C. Clasper, *J. R. Army Med. Corps* **2014**, *161*, 315.

[3] E. M. Shore, F. S. Kaplan, *Nat. Rev. Rheumatol.* **2010**, *6*, 518.

[4] M. A. J. B. K. Potter, L. J. A. Forsberg, T. A. Davis, C. P. T. K. N. Evans, M. A. J. J. S. Hawksworth, D. Tadaki, T. S. Brown, N. J. Crane, M. A. J. T. C. Burns, C. P. T. F. P. O'Brien, C. D. R. E. A. Elster, *J. Bone Jt. Surg.* **2010**, *92*, 74.

[5] B. K. Potter, T. C. Burns, A. P. Lacap, R. R. Granville, D. A. Gajewski, *J. Bone Jt. Surg.* **2007**, *89*, 476.

[6] M. P. Sullivan, S. J. Torres, S. Mehta, J. Ahn, *Bone Jt. Res.* **2013**, *2*, 51.

[7] R. H. Wittenberg, U. Peschke, U. Botel, *J. Bone Jt. Surg., Br. Vol.* **1992**, *74-B*, 215.

[8] J. Thilak, J. J. Panakkal, T.-Y. Kim, S. M. Goodman, S.-S. Lee, E. A. Salvati, *J. Arthroplasty* **2015**, *30*, 2304.

[9] T. N. Board, A. Karva, R. E. Board, A. K. Gambhir, M. L. Porter, *J. Bone Jt. Surg., Br. Vol.* **2007**, *89*, 434.

[10] T. Katagiri, K. Osawa, S. Tsukamoto, M. Fujimoto, A. Miyamoto, T. Mizuta, *Jpn. Dent. Sci. Rev.* **2015**, *51*, 42.

[11] D. M. Ramirez, M. R. Ramirez, A. M. Reginato, D. Medici, *Histol. Histopathol.* **2014**, *29*, 1281.

[12] L. Kan, Y. Liu, T. L. McGuire, D. M. P. Berger, R. B. Awatramani, S. M. Dymecki, J. A. Kessler, *Stem Cells* **2009**, *27*, 150.

[13] L. Lin, Q. Shen, T. Xue, C. Yu, *Bone* **2010**, *46*, 425.

[14] E. F. McCarthy, M. Sundaram, *Skeletal Radiol.* **2005**, *34*, 609.

[15] B. M. Isaacson, A. A. Brown, L. B. Brunker, T. F. Higgins, R. D. Bloebaum, *J. Surg. Res.* **2011**, *167*, e163.

[16] X. Liu, H. Kang, M. Shahnazari, H. Kim, L. Wang, O. Larm, L. Adolfsson, R. Nissenson, B. Halloran, *J. Orthop. Res.* **2014**, *32*, 183.

[17] T. Ueno, T. Kagawa, M. Kanou, T. Fujii, J. Fukunaga, N. Mizukawa, T. Sugahara, T. Yamamoto, *J. Cranio-Maxillofac. Surg.* **2003**, *31*, 356.

[18] V. Y. Lounev, R. Ramachandran, M. N. Wosczyna, M. Yamamoto, A. D. A. Maidment, E. M. Shore, D. L. Glaser, D. J. Goldhamer, F. S. Kaplan, *J. Bone Jt. Surg., Am. Vol.* **2009**, *91*, 652.

**ADVANCED
SCIENCE NEWS**

www.advancedsciencenews.com

**ADVANCED
BIOSYSTEMS**

www.adv-biosys.com

[19] L. Kan, J. A. Kessler, *J. Biomed. Biotechnol.* **2011**, *2011*, 309287.

[20] L. Claes, S. Recknagel, A. Ignatius, *Nat. Rev. Rheumatol.* **2012**, *8*, 133.

[21] F. Matassi, L. Nistri, D. Chicon Paez, M. Innocenti, *Clin. Cases Miner. Bone Metab.* **2011**, *8*, 21.

[22] H. Chang, M. L. Knothe Tate, *Stem Cells Transl. Med.* **2012**, *1*, 480.

[23] S. W. Kim, P. D. Pajevic, M. Selig, K. J. Barry, J. Y. Yang, C. S. Shin, W. Y. Baek, J. E. Kim, H. M. Kronenberg, *J. Bone Miner. Res.* **2012**, *27*, 2075.

[24] M. Li, N. Amizuka, K. Oda, K. Tokunaga, T. Ito, K. Takeuchi, R. Takagi, T. Maeda, *Microsc. Res. Tech.* **2004**, *64*, 330.

[25] J. Fang, B. K. Hall, *Dev. Biol.* **1996**, *180*, 701.

[26] V. S. Kumar, N. Barwar, S. A. Khan, *Ind. J. Orthop.* **2014**, *48*, 255.

[27] D. Eyrich, F. Brandl, B. Appel, H. Wiese, G. Maier, M. Wenzel, R. Staudenmaier, A. Goepferich, T. Blunk, *Biomaterials* **2007**, *28*, 55.

[28] D. Eyrich, A. Göpferich, T. Blunk, Fibrin in *Tissue Engineering*, (Ed.: J. P. Fisher), Springer, Boston, MA, **2007**, pp. 379–392.

[29] P. A. Janmey, J. P. Winer, J. W. Weisel, *J. R. Soc., Interface* **2009**, *6*, 1.

[30] R. M. Pidaparti, D. B. Burr, *J. Biomech.* **1992**, *25*, 869.

[31] A. L. Boskey, *BoneKEy Rep.* **2013**, *2*, 447.

[32] M. D. Morris, G. S. Mandair, *Clin. Orthop. Relat. Res.* **2011**, *469*, 2160.

[33] M. S. A. Johnsson, G. H. Nancollas, *Crit. Rev. Oral Biol. Med.* **1992**, *3*, 61.

[34] S. Ban, T. Jinde, J. Hasegawa, *Dent. Mater. J.* **1992**, *11*, 130, 217.

[35] T. Kani, M. Kani, Y. Moriwaki, Y. Doi, *J. Dent. Res.* **1983**, *62*, 92.

[36] E. D. Eanes, J. L. Meyer, *Calcif. Tissue Res.* **1977**, *23*, 259.

[37] N. J. Crane, V. Popescu, M. D. Morris, P. Steenhuis, M. A. Ignelzi Jr., *Bone* **2006**, *39*, 434.

[38] N. J. Crane, E. Polfer, E. A. Elster, B. K. Potter, J. A. Forsberg, *Bone* **2013**, *57*, 335.

[39] W. Denk, J. H. Strickler, W. W. Webb, *Science* **1990**, *248*, 73.

[40] X. Chen, O. Nadiarynkh, S. Plotnikov, P. J. Campagnola, *Nat. Protoc.* **2012**, *7*, 654.

[41] A. M. Phillips, *Injury* **2005**, *36*, S5.

[42] T. A. Franz-Odendaal, B. K. Hall, P. E. Witten, *Dev. Dyn.* **2006**, *235*, 176.

[43] S. L. Dallas, L. F. Bonewald, *Ann. N. Y. Acad. Sci.* **2010**, *1192*, 437.

[44] K. E. S. Poole, R. L. van Bezooijen, N. Loveridge, H. Hamersma, S. E. Papapoulos, C. W. Löwik, J. Reeve, *FASEB J.* **2005**, *19*, 1842.

[45] I. Kalajzic, B. G. Matthews, E. Torreggiani, M. A. Harris, P. D. Pajevic, S. E. Harris, *Bone* **2013**, *54*, 296.

[46] L. F. Bonewald, *J. Bone Miner. Res.* **2011**, *26*, 229.

[47] K. Zhang, C. Barragan-Adjemian, L. Ye, S. Kotha, M. Dallas, Y. Lu, S. Zhao, M. Harris, S. E. Harris, J. Q. Feng, L. F. Bonewald, *Mol. Cell. Biol.* **2006**, *26*, 4539.

[48] L. C. Bonar, A. H. Roufosse, W. K. Sabine, M. D. Grynpas, M. J. Glimcher, *Calcif. Tissue Int.* **1983**, *35*, 202.

[49] A. A. Gorustovich, *Microsc. Microanal.* **2010**, *16*, 132.

[50] P. Schneider, M. Meier, R. Wepf, R. Müller, *Bone* **2010**, *47*, 848.

[51] F. Peyrin, P. Dong, A. Pacureanu, M. Langer, *Curr. Osteoporosis Rep.* **2014**, *12*, 465.

[52] M. Langer, A. Pacureanu, H. Suhonen, Q. Grimal, P. Cloetens, F. Peyrin, *PLoS One* **2012**, *7*, e35691.

[53] Y. Kato, J. J. Windle, B. A. Koop, G. R. Mundy, L. F. Bonewald, *J. Bone Miner. Res.* **1997**, *12*, 2014.

[54] F. Boukhechba, T. Balaguer, J.-F. Michiels, K. Ackermann, D. Quincey, J.-M. Bouler, W. Pyerin, G. F. Carle, N. Rochet, *J. Bone Miner. Res.* **2009**, *24*, 1927.

[55] Q. Sun, Y. Gu, W. Zhang, L. Dziopa, J. Zilberberg, W. Lee, *Bone Res.* **2015**, *3*, 15026.

[56] K. Shimono, W.-e. Tung, C. Macolino, A. H.-T. Chi, J. H. Didizian, C. Mundy, R. A. Chandraratna, Y. Mishina, M. Enomoto-Iwamoto, M. Pacifici, M. Iwamoto, *Nat. Med.* **2011**, *17*, 454.

[57] F. S. Kaplan, E. M. Shore, *Nat. Med.* **2011**, *17*, 420.

[58] P. B. Yu, D. Y. Deng, C. S. Lai, C. C. Hong, G. D. Cuny, M. L. Bouxsein, D. W. Hong, P. M. McManus, T. Katagiri, C. Sachidanandan, N. Kamiya, T. Fukuda, Y. Mishina, R. T. Peterson, K. D. Bloch, *Nat. Med.* **2008**, *14*, 1363.

1700156 (12 of 12)